







Cite this: *Nanoscale*, 2023, **15**, 10651

Modulation of plasmonic chiral shell growth on gold nanorods *via* nonchiral surfactants†

Xinshuang Gao,^{a,b} Qiang Zheng,^{a,b} Hanbo Li,^{a,b} Chenqi Zhang,^{a,b} Rui Cai,^{a,b} Yinglu Ji,^a Zhijian Hu^a and Xiaochun Wu^{a,b}    

Recently, in combination with seed-mediated growth, thiolated chiral molecule-guided growth has shown great promise in obtaining chiral plasmonic nanostructures. Previously, with the assistance of chiral cysteines (Cys), we realized helical growth of plasmonic shells on gold nanorod (AuNR) seeds dispersed in cetyltrimethylammonium bromide (CTAB) solution. Herein, we further studied the roles of non-chiral cationic surfactants in tuning the helical growth. Both the counter anion and the hydrocarbon chain length of the surfactants were found to affect the formation of helical shells greatly. In particular, we exhibited surfactant-modulated conversion of the chiral shell deposition mode between layer growth and island growth. By optimizing growth conditions, an obvious plasmonic circular dichroism (PCD) response could be achieved for the island helical shell. Our findings demonstrated promising potential of nano-chemical synthesis in fabricating chiral plasmonic nanostructures with small structural sizes.

Received 24th March 2023,

Accepted 22nd May 2023

DOI: 10.1039/d3nr01371e

rsc.li/nanoscale

Introduction

Plasmonic nanomaterials possess unique surface plasmonic features that make them highly versatile in several fields, including optical sensing, imaging, metamaterial-based devices, and disease theranostics. The controlled chemical synthesis of plasmonic nanoparticles (PNPs) has led to the emergence of chemical nanoplasmonics, a new interdisciplinary branch of nanoscale chemistry and plasmonics that has garnered significant attention.¹ In this rapidly advancing field, nanochemistry-driven chiropasmonics has achieved exciting progress.^{2,3} Initially, the strong local electromagnetic field of the PNPs was introduced to enhance the chiroptical activities of chiral molecules anchored close to or on the surface of the achiral PNPs. Benefiting from the enhanced chiral molecule-plasmon interaction, the chiroptical activity of the PNPs at local plasmons, for instance, plasmonic circular dichroism (PCD), was also observed. Subsequently, modulating this interaction has become a useful way to regulate the chiroptical responses of the PNPs themselves. The chiroptical activity of chiral PNPs has been demonstrated across a broad spectral range, from UV-visible to near-infrared,^{3–5} making it highly attractive and useful for applications such as sensing,^{6–10}

enantio-differentiation,¹¹ circularly polarized photocatalysis,¹² disease treatment,^{13–15} and more. In addition, chiral plasmonic nanomaterials offer new perspectives to the traditional chirality field.

Despite significant efforts, the chiral molecule-plasmon interaction has limited the PCD responses of the PNPs. Strong PCD responses are primarily obtained from chiral assemblies of achiral PNPs using chiral molecule-guided assembly methods such as amino acids and peptides,^{16–20} polymers,^{21–25} and DNA.^{26–29} Discrete PNPs with an obvious chiral morphology have been limited to top-down methods with large structural sizes. Nevertheless, recent advancements in wet-chemical synthesis have made it possible to chemically prepare discrete chiral PNPs with smaller structure sizes.^{30–46} Nam and co-workers pioneered the preparation of discrete chiral PNPs with strong PCD responses by using seed-mediated growth guided by thiolated chiral amino acids or peptides to produce novel 432 Au helicoids on Au nanocube seeds.³⁰ This strategy has led to the development of more chiral plasmonic nanostructures such as helical plasmonic shells on gold nanorods (AuNRs),^{34,35} Au chiral propellers on Au nanoplates,³⁶ and chiral plasmonic triangular nanorings,³⁷ demonstrating the great potential of wet-chemical synthesis in producing discrete chiral nanostructures. In contrast, Liz-Marzán and co-workers showed that soft chiral template-directed overgrowth could also induce chiral growth of plasmonic nanomaterials, using chiral wrinkles formed by weak non-covalent interactions between chiral co-surfactants and achiral surfactants to obtain chiral Au nanostructures on AuNRs.³⁸

^aCAS Key Laboratory of Standardization and Measurement for Nanotechnology, National Center for Nanoscience and Technology (NCNST), Beijing 100190, P. R. China. E-mail: wuxc@nanoctr.cn

^bUniversity of Chinese Academy of Science, Beijing 100049, P. R. China

† Electronic supplementary information (ESI) available. See DOI: <https://doi.org/10.1039/d3nr01371e>



Although significant progress has been made in the field, controlling chiral growth remains a challenge due to the complex growth process.^{32,39} It is well-known that surfactants play a crucial role in the synthesis of noble metal NPs, particularly in seed-mediated growth,^{47–50} where quaternary alkylammonium halide surfactants are often used to modulate the shapes of Au NPs by influencing growth kinetics or selective binding of specific facets.^{51,52}

Despite complicated interplay of different mechanisms,^{53,54} both the hydrophobic chain length^{55,56} and halide counter ions of surfactants^{57–63} have been found to be useful in the morphology control of noble metal NPs. However, the formation of a chiral morphology remains an uncharted territory, and undoubtedly, surfactants will play an important role in this process.

Recently, we synthesized helical plasmonic nanorods using AuNR-mediated growth with the assistance of chiral cysteines.⁶⁴ Herein, we delved deeper into the roles of non-chiral surfactants in the formation of chiral shells and the possible tuning mechanisms by varying the counter ions and hydrocarbon chain lengths of cationic surfactants. Apart from previously employed cetyltrimethylammonium bromide (CTAB), an additional three other surfactants, cetyltrimethylammonium chloride (CTAC), octadecyltrimethylammonium bromide (OTAB) and octadecyltrimethylammonium chloride (OTAC), were employed. It was found that both the alkyl chain length and the halide ion affected the growth of the chiral shell, with the shell deposition mode primarily controlled by the counter anions. When bromide ions are used as counter ions, such as in the case of CTAB or OTAB, the shell growth

mainly occurs *via* a layer growth mode. In contrast, when changed to chloride ions, such as in the case of CTAC and OTAC, the island growth mode is dominant for the shell growth. Both counter ions and hydrocarbon chain length influence chiral growth *via* affecting Cys coverage on the metal surface. By tuning the growth conditions, the shell growth mode can be switched between the two growth modes.

Results and discussion

AuNR@Cys50-Ag_{0.35}Au_{0.65} nanostructures mediated by different surfactants

To explore the effect of non-chiral surfactants, we first employed the optimized growth conditions for the helical AuAg shell obtained in CTAB-mediated growth.⁶⁴ AuNRs (93 nm × 15 nm) with an LSPR maximum at ~1000 nm were used as seeds (Fig. S1†). After the shell growth, the obtained extinction spectra can be roughly divided into two groups as shown in Fig. 1A. CTAB- and OTAB-mediated growth belonged to one group, and the obtained plasmonic nanostructures showed well-separated transverse and longitudinal SPR bands. For the CTAB-mediated growth, the plasmonic nanostructures had the TSPR and LSPR maximized at 545 nm and 726 nm, respectively. The LSPR/TSPR intensity ratio was ~0.93. In the case of OTAB, these two bands blue-shifted to 535 nm and 695 nm, respectively, with a slightly increased LSPR/TSPR intensity ratio of ~1.05. CTAC- and OTAC-mediated growth fell into the other group, where the obtained plasmonic nanostructures exhibited greatly reduced and broadened LSPR



Fig. 1 Achiral surfactant-mediated chiral growth of AuNR@AuAg nanostructures. (A) Extinction spectra, (B) CD spectra, (C) g_{\max} values at the plasmon band and 370 nm band, and TEM images (D and E) of AuNR(30)@Cys(50)-Sur(15)-Ag_{0.35}Au_{0.65}(0.2) nanostructures mediated by four surfactants. AuAg alloy shell growth conditions: [AuNR] = 30 pM, [Sur] = 15 mM, [Cys] = 50 μM, [Ag⁺] = 0.03 mM, [Au³⁺] = 0.17 mM, [AA]/[Au³⁺ + Ag⁺] = 1.6 at the growth temperature of 60 °C for 1 h. Scale bar: 50 nm. Inset: lines were added to guide helical grooves in the rod marked in the frame for clarity.



responses without obvious peaks. For the CTAC-mediated growth, a broad plasmonic band centered at ~ 545 nm dominated the extinction spectrum. In the case of OTAC, the TSPR maximum blue-shifted to ~ 515 nm and was separated from the broad LSPR response. In addition, an absorption band centered at ~ 370 nm appeared, which came from small Au nanoclusters, formed *via* the reduction of the Au(I)-Cys complex by AA.⁶⁵ Correspondingly, the plasmonic CD responses were also divided into two groups with strong PCD responses for the CTAB/OTAB group and very weak PCD responses for the CTAC/OTAC group (Fig. 1B). The g factor value of the PCD_{max} followed the order of CTAB > OTAB >> OTAC > CTAC. The g_{max} value was -0.012 at 604 nm for CTAB, -0.0066 at 600 nm for OTAB, -6.8×10^{-4} at 685 nm for OTAC, and -7.6×10^{-5} at 665 nm for CTAC, respectively (see Fig. 1C and Fig. S2† for g factor spectra). The 370 nm band also showed a CD signal, indicating the formation of chiral Au nanoclusters.

In order to gain more insight into the PCD responses, we checked the morphologies of the obtained plasmonic nanostructures using TEM (Fig. 1D). Two different shell growth modes could be visualized. For CTAB- or OTAB-mediated growth, the plasmonic shell mainly exhibited the layer growth mode, showing regular shell shapes. For the OTAB-mediated growth, the overall morphology was similar to that of the CTAB-mediated growth⁶⁴ with more pitches. The mean rod length and width were 97 nm and 49 nm, respectively, for the CTAB-mediated growth, which became $103 \text{ nm} \times 45 \text{ nm}$ for the OTAB-mediated growth. For both surfactants, more metal deposited on rod sides, which led to an obvious reduction in the aspect ratio. The blue-shifted LSPR band with enhanced intensity agreed with shallower helical grooves observed for OTAB-

mediated growth, compared to their counterparts mediated by CTAB. The measured pitch depth was roughly 9.0 ± 2.0 nm and 3.9 ± 1.2 nm for CTAB- and OTAB-mediated growth, respectively. In contrast, for CTAC- or OTAC-mediated growth, the island growth was obvious. In the case of CTAC, the island growth was inhomogeneous. Large particles composed of small particles were found to distribute at different sites (endcaps, middle parts) of the AuNR seed. On some rods, helical arrangements of the particles on the rod can be visualized (Fig. 1E inset). Such structural features agreed with the observed extinction features. The dominant plasmon band at 545 nm can be ascribed to the large particles. Therefore, the counter ions of surfactants played a vital role in tuning shell growth mode. In the case of OTAC-mediated growth, the helical shells were composed of homogeneously distributed NPs. This indicated that the chain length can be used to improve shell deposition. Taken together, both the carbon chain length and the counter ion of the surfactants affect the growth of plasmonic shells and PCD responses of the obtained plasmonic nanostructures. The effect of the counter ion is stronger than that of the carbon chain length.

Improving PCD responses in OTAC-mediated chiral growth

As shown above, the OTAC-mediated growth could lead to homogeneous island growth of the shell with discernable helical nanostructures. It is therefore interesting to know whether the island growth mode can induce the strong PCD response. We first investigated the effect of Cys amount on the formation of the helical shell by fixing other growth parameters (Fig. 2 and Fig. S3†). In the absence of Cys, the obtained nanostructures showed typical plasmonic features of a rod-like morphology with the TSPR band and LSPR band



Fig. 2 Effect of Cys concentration on the formation of island helical shells mediated by OTAC (15 mM). (A) Extinction and (B) CD spectra. Inset: g_{max} vs. Cys concentration. (C) Typical TEM images of AuNR(30)@Cys(X)-OTAC(15)-Ag_{0.35}Au_{0.65}(0.2) nanostructures obtained at different Cys concentrations. Scale bar: 100 nm.



centered at 497 nm and 750 nm, respectively (Fig. 2A). The obtained nanostructures exhibited a very weak M-type PCD signal (~ 5 mdeg at 580 nm), which was opposite in sign to the Cys-mediated PCD signal (Fig. 2B). The g_{\max} factor value at 580 nm was 5.3×10^{-4} . The TEM image indicated a shallow sawtooth-like shell structure (Fig. 2C). In the zoomed image, helical features were visible, suggesting the formation of local chiral structures (Fig. 2C inset). In the presence of Cys, the plasmonic features changed greatly. At 10 μM Cys, the TSPR band red-shifted to 510 nm, whereas the LSPR band red-shifted to 923 nm with significant damping in intensity. The obtained nanostructures showed a weak P-type PCD signal.

TEM images exhibited the shell composed of compact nanoislands. On further increasing the Cys amount from 20 μM to 75 μM , the extinction spectra showed continuous damping and broadening of both LSPR (around 980 nm) and TSPR bands (around 520 nm). The shell deposition amount also decreased with Cys concentration. At the fixed AuNR concentration, the change in the extinction value in the 350–450 nm spectral range can be used to indicate the deposition amount of the shell.⁶⁶ Considering that the 370 nm band might interfere with the absorbance at 400 nm, we used the extinction value at 420 nm ($\text{Ext}_{420 \text{ nm}}$). The deposition amount of the shell at 75 μM Cys was nearly half of that in the absence of Cys. A 370 nm absorbance band began to appear at 20 μM Cys and gradually enhanced with the Cys amount. At all employed Cys concentrations, the PCD responses were weak (Fig. 2B). On increasing the Cys concentration, the g_{\max} value gradually increased, verifying the key role of Cys in guiding the helical growth of the shell (Fig. 2B inset). TEM images (Fig. 2C) exhibited more obvious helical twisting of the shell

around the AuNR seed by increasing the Cys amount. For instance, at 75 μM Cys, the obtained nanostructure could be considered as the AuNR wound by a helical coil. However, strongly damped SPR bands posed a limit to improving PCD responses by increasing the Cys amount.

In order to mitigate the damping of local plasmons at high [Cys], we investigated the effect of OTAC amount at a moderate Cys concentration of 40 μM . Increasing the OTAC amount from 15 mM to 100 mM led to the enhancement of the LSPR response and the decline of the shell deposition amount. In particular, with 100 mM OTAC, the intensity of the LSPR band centered at ~ 900 nm was stronger than that of the TSPR band centered at ~ 520 nm (Fig. 3A). With 100 mM OTAC, the deposition amount of the shell was 57% of that with 1 mM OTAC. On increasing the OTAC concentration, the 370 nm band gradually decreased, indicating decreased complexing of Cys with Au(i). The g_{\max} value vs. OTAC concentration showed a volcano-like shape (Fig. 3B inset and Fig. S4†), with the highest PCD response at an OTAC concentration of around 45 mM. With 1 mM OTAC, despite a high [Cys]/[OTAC] molar ratio of 4×10^{-2} , the obtained nanostructure exhibited no obvious PCD response. TEM images demonstrated that on increasing the OTAC amount, the shell structure changed from compact islands and loose coils to specific facet-exposed shells, indicating the conversion of the shell growth from the island growth mode to the layer growth mode. In comparison with Fig. 2, changing the OTAC amount was a feasible way to control local SPR features. Overall, changing the OTAC amount can be used to modulate shell deposition mode and it improves the PCD responses for island-like shells, which may benefit applications related to narrow plasmonic gaps and small NP sizes.



Fig. 3 Effect of OTAC concentration on the growth of the helical shell for AuNR(30)@Cys(40)-OTAC(X)-Ag_{0.35}Au_{0.65}(0.2). (A) Extinction and (B) CD spectra. Inset in B: g_{\max} vs. OTAC concentration. (C) TEM images. Scale bar: 100 nm.



Tuning the growth temperature (T) is a simple way to modulate shell deposition kinetics. By altering growth T , both the shell deposition amount and the PCD response were affected (Fig. 4A and Fig. S5†). On raising growth T from 30 °C to 60 °C, the $\text{Ext}_{420 \text{ nm}}$ value increased, suggesting enhanced metal ion reduction at elevated growth temperature. PCD responses were also raised by increasing growth T . The g_{max} value increased roughly in a linear manner with T from 30 °C to 70 °C (Fig. S5C†). The g_{max} value obtained at the growth T of 30 °C was -0.0019 at $\sim 790 \text{ nm}$, whereas it increased to -0.0062 at $\sim 660 \text{ nm}$ at the growth T of 70 °C. The 370 nm band was also mediated by the growth T , which was weak at 30 °C and at 70 °C. From TEM images, we observed a more regular helical shell upon elevating growth T .

At fixed concentration of total metal ions, changing AuNR concentration can vary the metal deposition amount per rod and thus provide a flexible way to tune shell thickness (Fig. 4B and Fig. S6†). By increasing AuNR seed concentration, the LSPR band was gradually enhanced. The PCD response showed a volcano-like dependence on rod concentration with optimal AuNR concentrations ranging from 45 pM to 75 pM. At the lowest rod concentration of 15 pM, the smallest g_{max} value was obtained (-0.0027 at 735 nm). The maximum g_{max} value of -0.0068 at 620 nm was obtained at 60 pM AuNRs. At the highest rod concentration of 150 pM, the g_{max} value was reduced to -0.004 at 550 nm. The valley peak of the PCD band could be continuously tuned from 735 nm to 520 nm by

increasing AuNR concentration. The TEM images exhibited a gradual conversion of the growth mode from the island growth to the layer growth mode upon increasing rod concentration.

At the fixed AuNR concentration, varying the concentration of added metal ions ($[\text{M}] = [\text{Au}^{3+}] + [\text{Ag}^{+}]$) creates a more straightforward way to control shell thickness. Under the given growth conditions, varying the total amount of metal ions from 0.05 mM to 0.3 mM led to a linear increase in the value of $\text{Ext}_{420 \text{ nm}}$, suggesting a quantitative deposition of the metal (Fig. S7†). The g_{max} value first rapidly increased with $[\text{M}]$, reached the maximum at 0.2 mM and 0.25 mM, and then slightly decreased upon further increasing $[\text{M}]$ to 0.25 mM (Fig. 4C and Fig. S7†). From the TEM images, we observed a transition of the shell growth mode from the layer mode at low $[\text{M}]$ to the island mode at high $[\text{M}]$, which agreed with the changes in plasmonic features from strong and narrow LSPR bands at the thin shell to broadened and damped ones at the thick shell.

In CTAB-mediated helical growth, we observed the positive effect of adding achiral thiols, such as 4-ATP, on improving chiral growth.⁶⁴ In OTAC-mediated growth, a small amount of 4-ATP could also improve the PCD response (Fig. S8†). For instance, a 1.5-fold enhancement in the g_{max} value was observed upon adding 2 μM 4-ATP. The TEM images indicated that a small amount of 4-ATP improved the helical structure. Owing to the competitive adsorption of Cys and 4-ATP, a

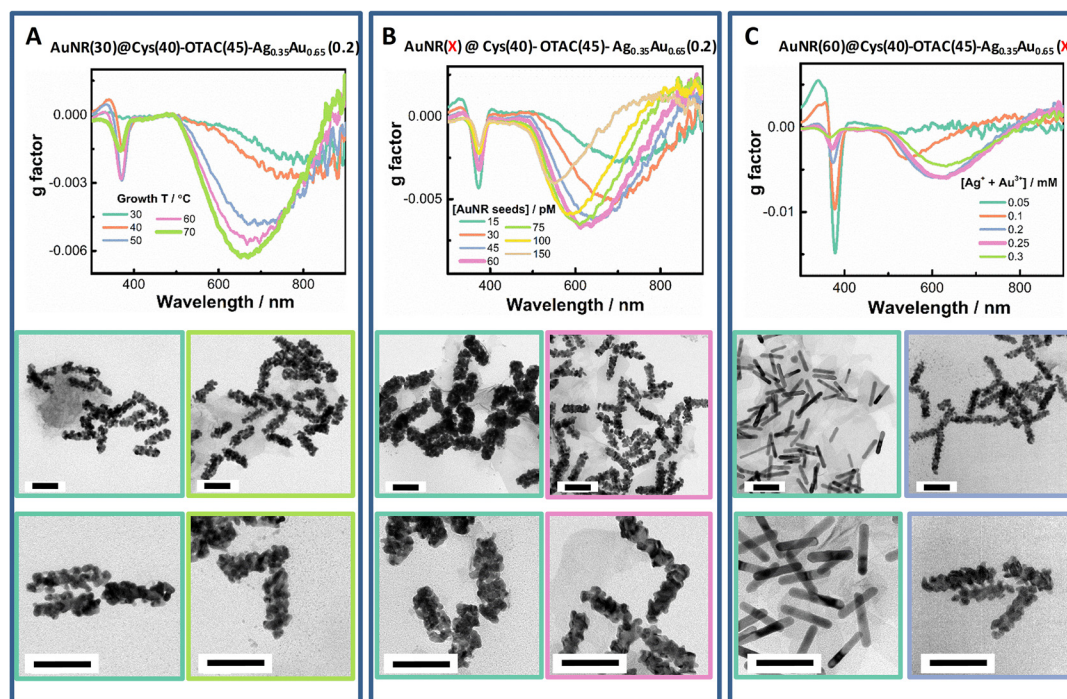


Fig. 4 Effects of other reaction parameters on the growth of the helical shell. (A) Effect of growth temperature: g factor spectra obtained at different growth temperatures and TEM images at growth temperatures of 30 °C and 70 °C, respectively. (B) Effect of AuNR seed concentration: g factor spectra at different AuNR concentrations and TEM images at the AuNR concentration of 15 pM and 60 pM, respectively. (C) Effect of shell thickness: g factor spectra obtained at different $[\text{Au}^{3+} + \text{Ag}^+]$ concentrations and TEM images at concentrations of 0.05 mM and 0.2 mM, respectively. TEM image scale bar: 100 nm.



higher concentration of 4-ATP decreased Cys adsorption and thus affected the chiral growth of the shell.

The effect of shell alloy composition revealed the importance of metal atom surface migration in the formation of the helical shell (Fig. S9†). At a total M of 0.2 mM, by varying the alloy composition from Ag 10% to 100%, the PCD response first increased, reached maximal responses at Ag contents ranging from 35% to 50%, and then reduced upon further increasing the Ag percentage. TEM characterization indicated that the helical shell structure was first enhanced and then reduced with the Ag percentage. This volcano dependence on the Ag percentage can be understood from the surface migration capability of the deposited metal. Au atoms diffuse slowly compared to Ag atoms. At a lower Ag percentage, properly enhanced atom migration may promote the formation of a more continuous helical shell. However, if the atom migration is too fast, before Cys adsorption, the deposited metal atoms tend to form a smooth surface driven by decreasing surface energy, as shown in the case of a pure Ag shell.

Tuning shell deposition mode by changing growth parameters

As shown in Fig. 1, the counter ions of the surfactants had a significant impact on the shell growth mode. With Br^- as the counter ion, the Cys-guided helical growth was dominated by the layer growth mode, as shown in CTAB- or OTAB-mediated growth. In contrast, with Cl^- as the counter ion, the island

growth mode was predominant, as observed in CTAC- and OTAC-mediated growth.

TEM characterization provided more information on the island-shell. The STEM image (Fig. 5A) showed that the AuNR seed was surrounded by the island-like shell. Element mapping exhibited homogeneous distribution of Au and Ag in the shell. The helical coil-like shell structure winding the AuNR was seen more clearly from the shape and contrast distribution of the TEM image for a typical core-shell nanostructure (Fig. 5B). The particle features of the helical shell were visualized from zoom-in HRTEM images (Fig. 5C and D), showing different orientations of nanodots around the AuNR seed. The appearance of Moiré patterns and differently oriented nanodots on the shell structure supported the island growth mode of the shell. Still, the AuNR seed and shell were dominated by a monocrystalline feature, as evidenced by their selected-area electron diffraction (SAED) pattern in the Fig. 5B inset and FFT patterns in Fig. 5E and F. This suggested that the alloy shell grew on the AuNR seed *via* the S-K mode. Some small dots (blue circle) in Fig. 5B indicated the existence of self-nucleation growth, such as the formation of Au nanoclusters or their aggregates. In contrast, the OTAB-mediated shell growth produced a good epitaxial shell *via* the layer growth mode (Fig. S10†).

The conversion of the shell growth mode can be understood from the effect of Cys adsorption on gold surface energy. The



Fig. 5 TEM characterization of AuNR(60)@Cys(40)-OTAC(45)-Ag_{0.35}Au_{0.65}(0.2). (A) STEM image and corresponding Au and Ag element mapping picture. (B) TEM image of one helical nanostructure. Inset: SAED pattern. (C and D) Zoom-in HRTEM images indicated in (B). (E) FFT patterns of marked regions in (C). (F) FFT patterns of marked regions in (D).



Cys covered gold surface shows reduced adhesion energy for Au atom deposition and thus can induce island growth mode. According to previous studies,⁶⁰ owing to the strong adsorption propensity of Br[−] to the Au surface, the CTAB adlayer on the Au surface is more compact than its CTAC counterpart. Hence, a high Cys coverage is more easily obtained on the CTAC-coated gold surface compared to that on its CTAB counterpart. On the other hand, compared to Br ions, weaker binding of gold ions with Cl ions leads to more easy Au deposition in the CTAC-mediated growth. The two effects were demonstrated by the shell growth in the absence of Cys (Fig. S11A†). Compared to CTAB- or OTAB-mediated growth, more metal deposition (Ext_{420nm}) was observed for CTAC- or OTAC-mediated growth after 60 °C for 1 h, and the diameter (*d*) of the nanostructures obtained in four surfactants followed the order of $d_{\text{CTAC}} > d_{\text{OTAC}} \cong d_{\text{CTAB}} > d_{\text{OTAB}}$. Upon increasing the hydrocarbon chain length (such as OTAC and OTAB), the shell growth was slowed down due to the increased adlayer packing order and enhanced metal ion binding by the micelle. In the absence of Cys, the shell deposition exhibited the layer growth mode in all four surfactants (Fig. S11B†), supporting the inhibition of metal deposition on the Cys-covered surface. Hence, the high Cys coverage on the CTAC-modified AuNR tends to induce the island growth mode. On changing to the OTAC-modified AuNR, benefiting from the improved packing order of the OTAC adlayer and reduced metal deposition, the controlled shell growth was achieved. The enhanced island growth was achieved by pre-incubation of AuNR seeds with Cys before the shell deposition. The sample with Cys pre-incubation exhibited more obvious island growth mode compared

with the sample without Cys pre-incubation and stronger PCD signals as well (Fig. S12†).

As shown above, surfactants affected the chiral shell growth mode *via* tuning Cys adsorption and metal deposition. During the metal deposition process, a proper Cys coverage on the shell surface is crucial to the formation of ordered helical structures. At low Cys coverage, the layer growth mode could be maintained. At high Cys coverage, the island growth mode is predominant. For the rational design of the helical growth, the proper match of Cys adsorption and metal deposition is needed. In general, slowing down the shell growth rate benefits the deposition of metal atoms under the guide of adsorbed Cys. For instance, increasing surfactant amount slows down metal deposition and reduces Cys adsorption, both of which promote the layer growth mode. On elevating the growth temperature, enhanced atom mobility may assist in the formation of the more ordered helical structures. Both strategies generate better helical shells *via* different ways. Owing to the complex interplay of different growth parameters, there is a non-trivial relationship between the growth parameters and PCD responses.

Volcano dependence of PCD responses on growth parameters

We observed a volcano-like relationship between the PCD response and some growth parameters, such as OTAC concentration, M amount, AuNR concentration, and AuAg alloy composition. This volcano relationship could be understood from the conversion of the shell growth mode and the structural ordering of the obtained helical shell. Taking OTAC amount as an example, increasing the OTAC concentration induced a



Fig. 6 Comparison of catalysis and SERS activity of chiral PNPs obtained from different growth modes. (A and B) Evolution of absorption spectra during NaA oxidation by H₂O₂ catalyzed by S1 and S2. (C) Catalytic rate comparison. (D) SERS spectra of 4-ATP on S1 and S2. (E) SERS intensity comparison. S1: AuNR(60)@Cys(40)-OTAC(45)-Ag_{0.35}Au_{0.65}(0.2) and S2: AuNR(30)@Cys(50)-CTAB(15)-Ag_{0.35}Au_{0.65}(0.2).

growth mode transition from the island growth to the layer growth mode. With 1 mM OTAC, a high [Cys]/[OTAC] ratio led to island growth. However, the fast metal deposition affected Cys adsorption and resulted in poor ordering of the helical island shell, which gave a weak PCD response. An appropriate increase of the OTAC amount slowed down metal deposition. Controlled Cys adsorption was achieved for good chiral growth. It led to the formation of a more ordered helical island shell for the large PCD response. On further increasing the OTAC concentration, the island growth mode was switched to the layer growth mode due to the decreased [Cys]/[OTAC] ratio. In this growth mode, the pitch depth is the key factor for the PCD response. A deeper pitch depth produced a larger PCD signal.⁶⁴ The obtained shallow pitch depth limited the chiroptical responses. Increasing the AuNR concentration also led to the evolution of the growth mode from the island mode at low AuNR concentration to the layer mode at high AuNR concentration. The small island sizes at low [AuNR] restricted the PCD response. The shallow pitch depth at high [AuNR] hindered the realization of high PCD. Similar trends were observed on varying the concentration of metal ions and alloy composition.

Due to different structural features, layer helical shells and island helical shells may find different application scenarios. Herein, the peroxidase-like activity of PNPs was evaluated using NaA oxidation by H₂O₂. In Fig. 6A, the absorbance of NaA at 264 nm reduced rapidly in the presence of S1 with the island shell. All of the added NaA was almost oxidized within 20 minutes. In contrast, for S2 with the layer shell at the same particle concentration, a large amount of added NaA remained unoxidized at 20 min (Fig. 6B). The oxidation rate of NaA (v_{NaA}) was 0.054 min⁻¹, 0.024 min⁻¹, and 0.014 min⁻¹ for S1, S2, and the control (without PNPs), respectively (Fig. 6C). Hence, S1 with the island shell exhibited better catalytic activity than S2 with the layer shell, agreeing with more active sites on the surface of small dots.

For the SERS activity measurement, 4-aminothiophenol (4-ATP) was used as the Raman probe. Upon 785 nm laser excitation, the observed Raman signals of 4-ATP from S1 were much weaker than those from S2 (Fig. 6D). For instance, at the two Raman characteristic bands of 4-ATP centered at 1086 cm⁻¹ and 1603 cm⁻¹, the Raman intensities from S2 were much stronger than those from S1 (Fig. 6E). The large SERS activity of S2 can be ascribed to its deep pitch depth (see Fig. 1D for a TEM image with CTAB), which produced strong local field enhancement.

Conclusions

Herein, the roles of achiral surfactants on the chiral growth of AgAu alloy shells on AuNR seeds were studied. Both the counter anion and the hydrocarbon chain length of the surfactants are found to affect the formation of helical shells greatly. With Cl⁻ as the counter ion, CTAC- and OTAC-mediated growth resulted in the island growth mode for the helical shell depo-

sition. Owing to strong island-island coupling, the obtained plasmonic nanostructures with the island shell are characterized with obviously damped local SPR features. Their counterparts with Br⁻ as the counter ion mainly induce the layer growth mode. During the shell growth, dynamic Cys coverage on the exposed metal surface determines the shell deposition mode. Generally, a high Cys coverage promotes the island growth mode, whereas the layer growth is maintained at a low Cys coverage. Based on this, we can intentionally tune the growth mode by controlling the adsorption of Cys *via* modulating various growth parameters, as demonstrated herein. For the rational design of the helical growth, during the metal deposition process, a proper Cys coverage is required to guide chiral growth, which can be achieved *via* the control of metal deposition and Cys adsorption. In the end, our findings demonstrate the important role of non-chiral surfactants in tuning helical growth, and give new insights for designing and synthesizing chiral nanostructures with expected optical properties using wet chemical synthesis. Considering the narrow gaps and small dot sizes, the core-shell plasmonic nanostructures with the helical island shell may find applications in enantiomeric discrimination and asymmetric catalysis.

Conflicts of interest

There are no conflicts to declare.

Acknowledgements

This work was supported by the National Natural Science Foundation of China (Grant No. 22072032), the National Key Research and Development Program of China (2021YFA1202803), and the Strategic Priority Research Program of Chinese Academy of Sciences (XDB36000000).

References

- 1 J. Nam, L. Liz-Marzán and N. Halas, *Acc. Chem. Res.*, 2019, **52**, 2995–2996.
- 2 M. Hentschel, M. Schaeferling, X. Duan, H. Giessen and N. Liu, *Sci. Adv.*, 2017, **3**, e1602735.
- 3 G. Zheng, J. He, V. Kumar, S. Wang, I. Pastoriza-Santos, J. Perez-Juste, L. M. Liz-Marzán and K. Y. Wong, *Chem. Soc. Rev.*, 2021, **50**, 3738–3754.
- 4 A. Guerrero-Martínez, J. L. Alonso-Gómez, B. Auguié, M. M. Cid and L. M. Liz-Marzán, *Nano Today*, 2011, **6**, 381–400.
- 5 J. Liu, L. Yang, P. Qin, S. Zhang, K. K. L. Yung and Z. Huang, *Adv. Mater.*, 2021, **33**, 2005506.
- 6 C. Hao, L. Xu, M. Sun, W. Ma, H. Kuang and C. Xu, *Adv. Funct. Mater.*, 2018, **28**, 1802372.
- 7 J. Kumar, H. Erana, E. Lopez-Martinez, N. Claes, V. F. Martin, D. M. Solis, S. Bals, A. L. Cortajarena,



- J. Castilla and L. M. Liz-Marzan, *Proc. Natl. Acad. Sci. U. S. A.*, 2018, **115**, 3225–3230.
- 8 J. Cai, C. Hao, M. Sun, W. Ma, C. Xu and H. Kuang, *Small*, 2018, **14**, 1703931.
- 9 T. Funck, T. Liedl and W. Bae, *Appl. Sci.*, 2019, **9**, 3006.
- 10 C. Hao, L. Xu, H. Kuang and C. Xu, *Adv. Mater.*, 2020, **32**, 1802075.
- 11 J. E. Lu, C. H. Yang, H. Wang, C. Yam, Z. G. Yu and S. Chen, *Nanoscale*, 2018, **10**, 14586–14593.
- 12 C. Hao, L. Xu, W. Ma, X. Wu, L. Wang, H. Kuang and C. Xu, *Adv. Funct. Mater.*, 2015, **25**, 5816–5822.
- 13 K. Hou, J. Zhao, H. Wang, B. Li, K. Li, X. Shi, K. Wan, J. Ai, J. Lv, D. Wang, Q. Huang, H. Wang, Q. Cao, S. Liu and Z. Tang, *Nat. Commun.*, 2020, **11**, 4790.
- 14 J. Wang, X. Wu, W. Ma and C. Xu, *Adv. Funct. Mater.*, 2020, **30**, 2000670.
- 15 F. Gao, M. Sun, W. Ma, X. Wu, L. Liu, H. Kuang and C. Xu, *Adv. Mater.*, 2017, **29**, 1606864.
- 16 S. Hou, T. Wen, H. Zhang, W. Liu, X. Hu, R. Wang, Z. Hu and X. Wu, *Nano Res.*, 2014, **7**, 1699–1705.
- 17 D. Meng, Y. Chen, Y. Ji, X. Shi, H. Wang and X. Wu, *Adv. Opt. Mater.*, 2020, **9**, 2001274.
- 18 M. Song, L. Tong, S. Liu, Y. Zhang, J. Dong, Y. Ji, Y. Guo, X. Wu, X. Zhang and R. Y. Wang, *ACS Nano*, 2021, **15**, 5715–5724.
- 19 W. Zhao, W. Zhang, R. Y. Wang, Y. Ji, X. Wu and X. Zhang, *Adv. Funct. Mater.*, 2019, **29**, 1900587.
- 20 J. Lu, Y. X. Chang, N. N. Zhang, Y. Wei, A. J. Li, J. Tai, Y. Xue, Z. Y. Wang, Y. Yang, L. Zhao, Z. Y. Lu and K. Liu, *ACS Nano*, 2017, **11**, 3463–3475.
- 21 X. Jin, J. Jiang and M. Liu, *ACS Nano*, 2016, **10**, 11179–11186.
- 22 R. Wang, J. Cui, X. Wan and J. Zhang, *Chem. Commun.*, 2019, **55**, 4949–4952.
- 23 G. Cheng, D. Xu, Z. Lu and K. Liu, *ACS Nano*, 2019, **13**, 1479–1489.
- 24 P. Szustakiewicz, N. Kowalska, D. Grzelak, T. Narushima, M. Gora, M. Baginski, D. Pocięcha, H. Okamoto, L. M. Liz-Marzan and W. Lewandowski, *ACS Nano*, 2020, **14**, 12918–12928.
- 25 N. A. Kotov, L. M. Liz-Marzán and P. S. Weiss, *ACS Nano*, 2021, **15**, 12457–12460.
- 26 A. Kuzyk, R. Schreiber, Z. Fan, G. Pardatscher, E. M. Roller, A. Hoge, F. C. Simmel, A. O. Govorov and T. Liedl, *Nature*, 2012, **483**, 311–314.
- 27 X. Lan, X. Lu, C. Shen, Y. Ke, W. Ni and Q. Wang, *J. Am. Chem. Soc.*, 2015, **137**, 457–462.
- 28 C. Shen, X. Lan, C. Zhu, W. Zhang, L. Wang and Q. Wang, *Adv. Mater.*, 2017, **29**, 1606533.
- 29 S. Liu, Y. Shang, Y. Jiao, N. Li and B. Ding, *Nanotechnology*, 2021, **32**, 402002.
- 30 H. E. Lee, H. Y. Ahn, J. Mun, Y. Y. Lee, M. Kim, N. H. Cho, K. Chang, W. S. Kim, J. Rho and K. T. Nam, *Nature*, 2018, **556**, 360–365.
- 31 H. Kim, S. W. Im, N. H. Cho, D. H. Seo, R. M. Kim, Y. C. Lim, H. E. Lee, H. Y. Ahn and K. T. Nam, *Angew. Chem., Int. Ed.*, 2020, **59**, 12976–12983.
- 32 H. E. Lee, R. M. Kim, H. Y. Ahn, Y. Y. Lee, G. H. Byun, S. W. Im, J. Mun, J. Rho and K. T. Nam, *Nat. Commun.*, 2020, **11**, 263.
- 33 N. H. Cho, H. E. Lee, H. Y. Ahn, Y. Y. Lee, S. W. Im, H. Kim and K. T. Nam, *Part. Part. Syst. Charact.*, 2019, **36**, 1900062.
- 34 S. Wang, L. Zheng, W. Chen, L. Ji, L. Zhang, W. Lu, Z. Fang, F. Guo, L. Qi and M. Liu, *CCS Chem.*, 2021, **3**, 2473–2484.
- 35 X. Wen, S. Wang, R. Liu, R. Duan, S. Hu, T. Jiao, L. Zhang and M. Liu, *Small*, 2022, **18**, 2104301.
- 36 Y. Ma, Z. Cao, J. Hao, J. Zhou, Z. Yang, Y. Yang and J. Wei, *J. Phys. Chem. C*, 2020, **124**, 24306–24314.
- 37 G. Wang, C. Hao, W. Ma, A. Qu, C. Chen, J. Xu, C. Xu, H. Kuang and L. Xu, *Adv. Mater.*, 2021, **33**, 2102337.
- 38 G. Gonzalez-Rubio, J. Mosquera, V. Kumar, A. Pedrazo-Tardajos, P. Llombart, D. M. Solis, I. Lobato, E. G. Noya, A. Guerrero-Martinez, J. M. Taboada, F. Obelleiro, L. G. MacDowell, S. Bals and L. M. Liz-Marzan, *Science*, 2020, **368**, 1472–1477.
- 39 N. H. Cho, G. H. Byun, Y. C. Lim, S. W. Im, H. Kim, H. E. Lee, H. Y. Ahn and K. T. Nam, *ACS Nano*, 2020, **14**, 3595–3602.
- 40 N. H. Cho, Y. B. Kim, Y. Y. Lee, S. W. Im, R. M. Kim, J. W. Kim, S. D. Namgung, H. E. Lee, H. Kim, J. H. Han, H. W. Chung, Y. H. Lee, J. W. Han and K. T. Nam, *Nat. Commun.*, 2022, **13**, 3831.
- 41 L. Xu, X. Wang, W. Wang, M. Sun, W. J. Choi, J. Y. Kim, C. Hao, S. Li, A. Qu, M. Lu, X. Wu, F. M. Colombari, W. R. Gomes, A. L. Blanco, A. F. de Moura, X. Guo, H. Kuang, N. A. Kotov and C. Xu, *Nature*, 2022, **601**, 366–373.
- 42 F. Wu, Y. Tian, X. Luan, X. Lv, F. Li, G. Xu and W. Niu, *Nano Lett.*, 2022, **22**, 2915–2922.
- 43 N. Zhang, H. Sun, S. Liu, Y. Xing, J. Lu, F. Peng, C.-L. Han, Z. Wei, T. Sun, B. Yang and K. Liu, *CCS Chem.*, 2022, **4**, 660–670.
- 44 N. Zhang, H. Sun, Y. Xue, F. Peng and K. Liu, *J. Phys. Chem. C*, 2021, **125**, 10708–10715.
- 45 G. Zheng, S. Jiao, W. Zhang, S. Wang, Q. Zhang, L. Gu, W. Ye, J. Li, X. Ren, Z. Zhang and K.-Y. Wong, *Nano Res.*, 2022, **15**, 6574–6581.
- 46 B. Ni, M. Mychinko, S. Gomez-Grana, J. Morales-Vidal, M. Obelleiro-Liz, W. Heyvaert, D. Vila-Liarte, X. Zhuo, W. Albrecht, G. Zheng, G. Gonzalez-Rubio, J. M. Taboada, F. Obelleiro, N. Lopez, J. Perez-Juste, I. Pastoriza-Santos, H. Colfen, S. Bals and L. M. Liz-Marzan, *Adv. Mater.*, 2023, **35**, 2208299.
- 47 T. Song, F. Gao, S. Guo, Y. Zhang, S. Li, H. You and Y. Du, *Nanoscale*, 2021, **13**, 3895–3910.
- 48 S. E. Lohse and C. J. Murphy, *Chem. Mater.*, 2013, **25**, 1250–1261.
- 49 L. Scarabelli, M. Coronado-Puchau, J. J. Giner-Casares, J. Langer and L. M. Liz-Marzan, *ACS Nano*, 2014, **8**, 5833–5842.
- 50 Y. Shi, Z. Lyu, M. Zhao, R. Chen, Q. N. Nguyen and Y. Xia, *Chem. Rev.*, 2021, **121**, 649–735.



- 51 M. L. Personick and C. A. Mirkin, *J. Am. Chem. Soc.*, 2013, **135**, 18238–18247.
- 52 Q. Wang, Z. Wang, Z. Li, J. Xiao, H. Shan, Z. Fang and L. Qi, *Sci. Adv.*, 2017, **3**, e1701183.
- 53 M. Grzelczak, J. Perez-Juste, P. Mulvaney and L. M. Liz-Marzan, *Chem. Soc. Rev.*, 2008, **37**, 1783–1791.
- 54 H. Kang, J. T. Buchman, R. S. Rodriguez, H. L. Ring, J. He, K. C. Bantz and C. L. Haynes, *Chem. Rev.*, 2019, **119**, 664–699.
- 55 J. Gao, C. M. Bender and C. J. Murphy, *Langmuir*, 2003, **19**, 9065–9070.
- 56 S. M. Shaban, J. Kang and D.-H. Kim, *Compos. Commun.*, 2020, **22**, 100537.
- 57 N. Garg, C. Scholl, A. Mohanty and R. Jin, *Langmuir*, 2010, **26**, 10271–10276.
- 58 M. R. Langille, M. L. Personick, J. Zhang and C. A. Mirkin, *J. Am. Chem. Soc.*, 2012, **134**, 14542–14554.
- 59 S. E. Lohse, N. D. Burrows, L. Scarabelli, L. M. Liz-Marzán and C. J. Murphy, *Chem. Mater.*, 2013, **26**, 34–43.
- 60 S. K. Meena, S. Celiksoy, P. Schafer, A. Henkel, C. Sonnichsen and M. Sulpizi, *Phys. Chem. Chem. Phys.*, 2016, **18**, 13246–13254.
- 61 S. Ghosh and L. Manna, *Chem. Rev.*, 2018, **118**, 7804–7864.
- 62 M. Brown and B. J. Wiley, *Chem. Mater.*, 2020, **32**, 6410–6415.
- 63 S. K. Meena and C. Meena, *Nanoscale*, 2021, **13**, 19549–19560.
- 64 J. Chen, X. Gao, Q. Zheng, J. Liu, D. Meng, H. Li, R. Cai, H. Fan, Y. Ji and X. Wu, *ACS Nano*, 2021, **15**, 15114–15122.
- 65 J. Yan, Y. Chen, S. Hou, J. Chen, D. Meng, H. Zhang, H. Fan, Y. Ji and X. Wu, *Nanoscale*, 2017, **9**, 11093–11102.
- 66 Z. Hu, S. Hou, Y. Ji, T. Wen, W. Liu, H. Zhang, X. Shi, J. Yan and X. Wu, *AIP Adv.*, 2014, **4**, 117137.

